Renewable Energy 210 (2023) 386–396

Contents lists available at ScienceDirect

Renewable Energy

journal homepage: www.elsevier.com/locate/renene

Nanopatterned indium tin oxide as a selective coating for solar thermal applications

Mahdi Motamedi [a,*], Guobin Jia [b], Yin Yao [c], Katie Shanks [d], Peyman Yousefi [e], Yasitha L. Hewakuruppu [a], Mehdi Rafeie [a,f], Florian Lindner [b], Robert Patterson [g], Silke Christiansen [e], Jonathan Plentz [b], Pramod Koshy [h], Robert A. Taylor [a,**]

[a] School of Mechanical and Manufacturing Engineering, University of New South Wales (UNSW), Sydney, NSW, 2052, Australia
[b] Leibniz Institute of Photonic Technology (LEIBNIZ IPHT), Albert-Einstein-Str. 9, 07745, Jena, Germany
[c] Mark Wainwright Analytical Centre, Electron Microscopy Unit, UNSW Sydney, Sydney, NSW, 2052, Australia
[d] Environment and Sustainability Institute, University of Exeter- Penryn Campus, Cornwall, TR10 9FE, UK
[e] Fraunhofer Institute for Ceramic Technologies and Systems IKTS, Äussere Nürnberger Strasse 62, Forchheim, 91301, Germany
[f] Lowy Cancer Research Centre, School of Medical Sciences, UNSW Sydney, Sydney, NSW, 2052, Australia
[g] School of Photovoltaic and Renewable Energy Engineering, UNSW Sydney, Sydney, NSW, 2052, Australia
[h] School of Materials Science and Engineering, UNSW Sydney, Sydney, NSW, 2052, Australia

ARTICLE INFO

Keywords:
Solar thermal
Double self-assembly
Etch mask deposition
Selective cover
Indium tin oxide
Etching

ABSTRACT

Indium tin oxide (ITO) coatings have been proposed to reduce thermal emission losses for solar thermal applications. Unfortunately, ITO *also* has a large amount of free charge carriers (~1×10^{20} per cm^3), which absorb sunlight. To address this issue, we propose a nano-patterned ITO-coated quartz exhibiting *both* anti-reflectivity (to maximize solar transmission) and low emissivity (to minimize long wavelengths radiative losses). A record small-size nanosphere (~60 nm) etch mask was prepared via double self-assembly, followed by dry etching and characterisation. In parallel, alternative nanopattern geometries were modelled using the Lumerical FDTD software to optimise short wavelength transmission without diminishing the inherently low emissivity of unetched ITO. It was found that an inverted moth's eye pattern (height = 250 nm and spacing = 80 nm) gave the best results at various solar concentrations (1 sun @ 100 °C, 10 suns @ 400 °C, and 100 suns @ 600 °C), resulting in ~7% improvement in the solar weighted transmission as well as a similar boost in the overall efficiency factor for selectivity. It was concluded that if the proposed deposition/etching processes can be cost-effectively scaled in a continuous process, it would provide a net performance boost for most solar thermal technologies.

1. Introduction

1.1. Solar thermal collectors

The cover of a solar thermal collector provides a critical 'window' into the overall efficiency of the collector. Although it may seem straightforward, the cover dictates how much sunlight transmits to the absorber *and* the bulk of the radiation and conduction heat losses leaving the solar collector (to the environment). In a typical solar collector, the cover is made of either low-iron glass or, in some cases, UV-resistant plastic [1,2]. Solar glasses can usually transmit more than 90% of incoming light, but they are typically not designed to stop the long wavelength emission from the absorber [3,4]. Thus, a typical low-iron glass has a large black body-weighted emittance, up to 87% [5]. This indicates that bare glass cannot be relied upon to manage outgoing thermal radiation. This may not be an issue for photovoltaic collectors (which operate better at lower temperatures [6]) or for solar thermal collectors which have a selective surface absorber (which controls long-wavelength emission at its source). However, the emerging technologies of photovoltaic/thermal (PVT) collectors and direct absorption solar collectors (DASCs) are often designed to operate at elevated temperatures and have relatively high (undesirable) radiation heat transfer losses [7]. For these systems, the cover serves as a final defence against radiation losses [8].

* Corresponding author.
** Corresponding author.
E-mail addresses: Motamedi.Mahdi66@Gmail.com (M. Motamedi), Robert.Taylor@UNSW.edu.au (R.A. Taylor).

https://doi.org/10.1016/j.renene.2023.04.020
Received 27 November 2022; Received in revised form 4 March 2023; Accepted 6 April 2023
Available online 12 April 2023

1.2. ITO coatings

Selectively transmitting materials (i.e., heat mirrors), have been employed for many years as architectural glazing and for various optical applications, but these are not optimised for transmitting the whole solar spectrum (which includes some IR wavelengths up to 2.5 μm) [7,8]. Table 1 provides an overview of these materials.

As can be noticed from Table 1, although it is a function of temperature and was not reported in all the studies, the lowest long wavelength emittance was 0.1. For the cover material, ideally, there should be 100% transmission in 0–2.5 μm and 100% reflection in 2.5–40 μm [7]. Obviously, this cannot be achieved in practice but Table 1 indicates two things. Firstly. majority of the studies focus on opaque surfaces while transparent surfaces are relatively under-investigated. Secondly, there is room for improvement in boosting transmission in 'long--wavelength emission control' coatings.

Overall, indium tin oxide, ITO (commonly fabricated via magnetron sputtering [15–18]), has compellingly shown to be the best 'selective transmitter' [7] when ranked against other transparent conducting oxides at a variety of solar concentrations and operating temperatures (100–600 °C) [20].

However, ITO has not yet been nanopatterned to improve the *overall* optical performance (from 0 to 40 μm) of solar thermal cover material.

1.3. Tunable subwavelength structures

Subwavelength structures (SWSs) represent an emerging approach achieving a high level of control over a material's optical properties. One of the applications of such structures is realising surfaces with the anti-reflective property. SWSs can be periodic (i.e., ordered in hexagonal or squared arrays [21]) or stochastic (i.e., random) [22]. The degree of order or randomness is very important when attempting to model such structures. Highly ordered structures can be modelled relatively accurately, whereas random SWSs are harder to predict [23]. It has also been reported that periodic SWSs result in less scattering loss compared to their random counterparts [24]. SWSs can have a wide range of shapes (domes, blocks, cones, pyramids, rods, pillars, etc.). Notably, tapered cones and rounded caps can be produced to be similar in morphology to natural moth-eye protuberances, which are essentially graded-index anti-reflective coatings [21,25]. Nano-rods or nano-pillars are also often reported in the literature due to their simpler fabrication (i.e., dry etching). Importantly, care must be taken to ensure that SWSs do not simply decrease reflection at the expense of lower transmission due to higher absorption (i.e., via multiple internal reflections), refraction loss, scattering loss, or any combinations of these factors [26]. The two most important design variables in a given SWS are structure height (h) and periodicity, (Λ), both of which critically influence optical performance [21–24,27–30].

With respect to the height (h), the seminal study by Clapham and Hutley [28] on the moth's eye structure, indicated that the ideal height is related to the wavelength(s) (λ) of interest, and can be characterised by a critical ratio of $h/\lambda \approx 0.4$ [28,29]. For the visible region, this limits the recommended height of ≥250 nm [28].

Regarding periodicity (Λ), an array of structures on a surface (depending on their size) may enable a coating to act as a selective grating on the surface [31]. When the periodicity is significantly less than the incident light's wavelength $\Lambda < \lambda$, the incident light only experiences the far-field, effective refractive index of the pattern (i.e., somewhere between air and the solid medium) [32]. It should be noted that the apparent size of the pattern may change based upon the incident angle, so to ensure effective transmission through the structure at oblique incident angles (of up to 60°), $\Lambda < 0.5\lambda/n$ (where n is the refractive index of the material) [29].

According to Table 1, there is no study on patterned ITO for solar thermal applications. Thus, in the current study, the aim is to pattern an ITO-coated glass cover.

1.4. Fabrication techniques

From a fabrication perspective, a smooth ITO surface has been patterned using either additive methods (e.g. pulsed laser deposition [14]) or subtractive methods (e.g., laser ablation [33] and etching [34]). To the authors' knowledge, the smallest ITO features that have been fabricated via wet etching in the literature were 250–1100 nm (i.e.,

Table 1
Overview of selective coatings, with emphasis on ITO-based films for solar applications.

Study Type	Film Composition	Fabrication Technique	Application	Results(s)	Reference
Exp.	GZO*	Sputtering and rapid thermal annealing	Thin film photovoltaics	• Film annealed at 570 °C showed the highest transmission	[9]
Exp.	TaTO**	Magnetron sputtering	High temperature solar thermal	• Optical and structural stability of the layer up to 1073 K in vacuum • The optimised layer stack had reflective losses of <0.05 and decreased the emissivity to <0.3.	[10]
Num. and Exp.	ITO vs. AZO***w/w/o an anti-reflective bottom layer	Manufactured by Euroglas, Germany	Single- and double-glazed flat plate solar collectors	• Solar transmittance: 0.83–0.86, normal emissivity: 0.19 and 0.30. • ITO beats AZO in chemical resistance and emittance while AZO beats ITO in economics and ecology.	[11,12]
Exp.	ITO thin films on glass	Femtosecond laser	Thin film photovoltaics	• Irradiation on both the top and bottom of micropatterned samples studied	[13]
Num. and Exp.	ITO-based	Pulsed laser deposition	High temperature solar selective absorber	• Solar absorptance: 0.76 • Thermal emittance: 0.12 at 800 °C • Cut-off wavelength: 1.7 μm	[14]
Num. and Exp.	ITO coating on Ta	Radio-frequency magnetron sputtering	High temperature solar selective absorber	• Hemispherical total emittance: 0.11 • Solar absorptance: 0.71	[15,16]
Exp.	ITO coated tungsten	Magnetron sputtering and interference lithography	High temperature solar selective absorber	• Cut-off wavelength: ~1.5 μm, • Hemispherical total emittance: 0.16 • Solar absorptance: 0.83	[17]
Num. and Exp.	ITO coated tungsten	Radio-frequency magnetron sputtering	High temperature solar selective absorber	• Identified optimal ITO properties • Solar absorptance: 0.95 • Hemispherical emittance: 0.10 at 973K.	[18]
Num.	Two ITO-based films	n/a	Parabolic trough evacuated collector tubes	• Less heat loss due to lower outer surface emissivity and higher inner surface reflectivity	[19]

*: Gallium-doped zinc oxide, **: Tantalum doped tin oxide, ***: Aluminium-doped zinc oxide.

sphere-shaped protrusions [35]). Since the peak of the solar spectrum occurs at ~530 nm and there is appreciable solar energy down to 250 nm (UV light), 250+ nm feature sizes will fail the $\Lambda < 0.5\lambda/n$ periodicity condition mentioned above, leading to a potential loss of solar transmission. Dry etching presents a potential pathway towards smaller feature sizes, and it can produce repeatable, uniform, high throughput patterns [36]. To achieve a nanopatterned sample using this technique, though, a small feature (<250 nm) etch mask layer must be produced first. Such an etch mask can be prepared through several methods such as in block co-polymer lithography [37,38], holographic lithography [39], nanosphere lithography [40], etc. Nanosphere lithography can exploit polymeric spheres (e.g., nanoparticles of polystyrene (PS)), but deposition of a *monolayer* of such small particles remains a challenge. Potentially reliable and scalable processes for nanosphere lithography are Langmuir-Blodgett (LB) deposition and double self-assembly (DSA) [41–43]. However, to the best of authors' knowledge, the smallest diameter size of PS spheres that have been deposited in a *monolayer* is ~200 nm [44,45]. In this study, we aim to *significantly push the small-scale limits* of this technology down to ~60 nm PS spheres. If achieved, ~60 nm feature size can ***pass*** the $\Lambda < 0.5\lambda/n$ periodicity condition for the short wavelength solar spectrum.

1.5. Modelling methods

Anti-reflective SWSs can be mathematically modelled via several methods such as effective medium theory (EMT) and finite-difference time-domain (FDTD) modelling [46]. The choice of method depends on the SWS under study and the parameters of interest (e.g., the porosity or the shape). For example, EMT is useful for modelling uniformly patterned SWSs. However, EMT loses accuracy for complex shapes or if randomised features are required, including those due to manufacturing error. There are also different EMT models such as the Bruggeman model which has a wider range of applicability than the Maxwell-Garnett model [47]. Stavenga et al. [48] used the Bruggeman [49] model to divide a paraboloid-shaped SWS into 100 layers to calculate the reflectance properties of moth eyes [48]. Choi et al. also used the Bruggeman EMT, but for tapered porous SWSs made of PMMA and ITO [50]. FDTD methods, which require computational modelling software, are increasingly being used to design and analyse the optical properties of complex SWSs in the literature [46]. This trend is likely due to the superior accuracy and versatility of FDTD methods in replicating specific geometries and non-uniform patterns, including representing "realistic" SWSs from imperfect manufacturing methods.

This study aims to model both the real nanopatterned ITO-based cover fabricated in this work along will a variety of related morphologies. Thus, the FDTD method was selected for the simulations since it can account for a wide range of geometries.

2. Simulative and experimental methods

As discussed in the Introduction, although patterning ITO via (sub-200 nm) nanosphere lithography has not been attempted, the geometry of the SWS pattern can be roughly fixed by the optimum values reported in the literature, which are dependent on the incident wavelength spectrum. As noted above, the particle diameter dictates the periodicity [40]. To minimise scattering loss the periodicity of desired SWSs in the current study was chosen as less than one tenth of the wavelength [51]. This section overviews the procedures for manufacturing the ITO samples, etch mask preparation (via self-assembly technique), the etching process, and the modelling.

2.1. Fabrication of ITO samples

The optical constants assumed for ITO were used as per a previous study from the co-authors [8]. To calculate the 'bulk' optical properties (i.e., transmission and reflection spectra), these constants were plugged into OpenFilters (a free optical analysis software [49]). These spectra were then supplied to an ITO manufacturer.

The ITO-coated quartz samples were fabricated with a batch-type magnetron sputtering machine (modified from Shincron) by ITO manufacturer GEOMATEC (Yokohama, Japan).

As might be expected, the fabricated ITO samples (a flat coating) did not exactly match the modelled flat ITO properties (via OpenFilters modelling) due to (three) fabrication limitations. Firstly, the OpenFilters model assumes uniform thickness and zero surface roughness, which does not occur in reality. Secondly, since ITO films are typically fabricated with high electrical conductivity for the electronics industry [52], the equipment has not been optimised for optical transmission (e.g., relatively low free carriers). Thirdly, contamination (from previous runs) and imperfect process control can lead to non-ideal optical properties [53].

2.1.1. Characterisation of the flat, unetched ITO

The first step in this study was the characterisation of the as-received unetched ITO (which was deposited on a quartz substrate) to determine the features (optical properties, surface structure, and roughness).

2.1.1.1. Optical properties. Ellipsometry measurements were used to obtain the optical constants of the flat, unetched ITO samples. This was done using two different instruments, an ellipsometer (a JA Woollam Variable Angle with a spectral range of 193–3200 nm) and an FTIR ellipsometer (a JA Woollam IR-VASE, with a spectral range of 1.6–40 μm). The modelling for the latter measurement was done using the commercial WVASE application from J.A. Woollam, which provided the optical constants along with the mean squared error (MSE). To model the optical constants of the former, the WVASE measurements were used with the Complete EASE software (also from J.A. Woollam). The optical constants obtained from the modelling were used for the FDTD simulations of the ITO SWSs. Additionally, the optical properties of the unetched ITO (transmission and reflection spectra) were measured using a PerkinElmer Lambda 1050 UV–VIS spectrophotometer (280–2500 nm).

2.1.1.2. Surface characterisation. The ITO samples were inspected to ensure that the samples could be safely prepared for further processing (i.e., etch mask deposition followed by etching). Scanning electron microscopy (SEM, FEI Nova NanoSEM 450 FE-SEM and FEI Nova NanoSEM 250 FE-SEM and Field Emission Scanning Electron Microscope JSM6700F from JEOL) and atomic force microscopy (AFM, Bruker Dimension ICON SPM) were used to analyse the surface structure and measure the surface roughness.

2.2. Etch mask preparation

The deposition of polystyrene on the ITO-coated substrate was carried out via double self-assembly (DSA).

2.2.1. Materials

Hexylamine (99%) and sodium dodecyl sulfate (SDS, >99.0%) were purchased at Sigma Aldrich. For the deposition of the monolayer of the PS nanospheres, high purity water with a resistance of 15.0 MΩ·cm (25 °C) was used, and it was prepared by a Milli-Q device.

Of the monodisperse bead available on the market, ~60 nm polystyrene (PS) beads (3000 Series Nanosphere STD 60 nm) were selected for the present study.

2.2.2. DSA technique

The deposition of the monolayer of hexagonally packed nanospheres was performed similarly to the process described in Ref. [42]. A schematic explanation of the DSA process is illustrated in Fig. 1. In this process, hexylamine functionalized PS nanospheres are distributed on

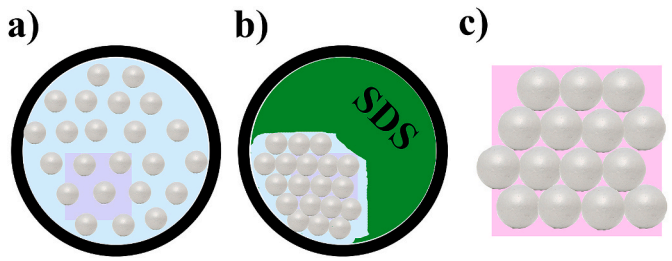

Fig. 1. Schematic view of the DSA process of the functionalized polystyrene nanospheres; a) PS nanospheres self-assembly on the water surface, where the lavender square depicts the sample placed beneath the water prior to the distribution of the PS nanospheres. b) SDS molecules push the PS nanospheres together to form a densely packed monolayer which can be deposited on the sample by pumping out of the water; c) Enlarged coated sample with a PS monolayer after drying.

the water surface by a syringe, forming a loosely packed monolayer. Then, ~100 μl of the 10 wt % SDS water solution was added at the edge of the Petri dish, so that the PS nanospheres will be pushed together during the spreading of the SDS molecules on the water surface, forming a densely packed (hexagonal) monolayer of PS. Next, the PS monolayer will be attached to the sample placed beneath as the water level drops by pumping out the water. This process relies on the pressure exerted by the SDS molecules to stabilize the PS monolayer, ensuring a reliable transfer of the monolayer. It should be noted that the PS nanospheres as well as the SDS molecules rearrange themselves (self-assembly) during the transfer, so by controlling the relative concentrations and process conditions, it is possible to produce a conformal coating of PS monolayer on complex 3D surfaces. Finally, after the deposition, the samples are dried in a furnace at 80 °C for 15 min to remove the dispersant (water). The quality of the prepared etch mask was investigated by taking several random SEM images from different spots of the samples.

2.3. Dry etching

After the deposition process (using the DSA technique), the ITO pattern can be produced by dry etching around the PS particles. In this study, a reactive ion etching tool (from Oxford Instruments - Plasmalab System 100) was employed, using a previously developed recipe based on [54] (i.e., with CH_4+H_2) and the values presented in Table 2.

2.3.1. Post-etching characterisation

The dry etched sample was optically characterised using a UV-VIS spectrophotometer (Cary 5000 UV-VIS-NIR, 175–3300 nm).

Several SEM images were taken to determine the surface structure after the etching. The etch depth was also estimated by removing a small area of the etched sample via focused ion beam (FIB) followed by SEM imaging.

2.4. SWS simulation and emittance calculation methods

An FDTD modelling software, Lumerical, was utilised to simulate the anti-reflective potential of 250 nm thick ITO patterns (i.e., the recommended height from Ref. [28]) with differing geometries (i.e. pillars, moth eyes, inverted moth eye, and holes). Fig. 2 below shows the range of options studied in this work along with the side-view schematic of the sample (i.e., 'Exp. Etched') which was experimentally etched (see subsection 3.3).

Table 2
The utilised dry etch recipe.

Parameter	Value	Unit
Gas Flow Rate	CH_4: 25, H_2: 10	sccm
Pressure	10	mTorr
RIE Power	150	W
ICP Power	500	W
Bias	513	V
Substrate Temperature	65	°C
Time	2	min.

To replicate the experimentally etched sample of ITO, where only partial etching was obtained, a three-layer system consisting of patterned ITO, ITO, and quartz was also simulated (see Fig. 3). A few geometries were compared here to investigate which represented the real etched sample and also to see if this stepped ITO layering could be more beneficial than a fully etched design. The outermost layer was assumed to be a patterned layer of 70 nm thick ITO, (as informed by Scanning Electron Microscopy of the etched sample see sub-section 3.3). Average known surface roughness was also measured on three random spots of the etched sample and the rough surface simulated within the FDTD software.

To choose between these options for the intended application of a solar thermal collector, the resultant reflection and transmission spectral curves for each design were used to calculate the solar weighted transmittance, T_{sol} (using Eqn. (1) below), and the black-body-weighted hemispherical emittance, E_{BB}, (using Eqn. (2) below). For the E_{BB} calculation, the spectral range of interest was kept wide, 280-40,000 nm, to account for emission at room temperature as well as elevated temperatures. Based upon T_{sol} and E_{BB}, a final figure of merit, efficiency factor for selectivity, the EFS (defined as Eqn. (4) below), was used, based upon prior work [7]:

$$T_{sol} = \frac{\int_{280}^{2500} T(\lambda)\, G(\lambda)\, d\lambda}{\int_{280}^{2500} G(\lambda)\, d\lambda} \tag{1}$$

$$E_{BB} = \frac{\int_0^{\infty} E(\lambda)\, I_{\lambda}^{BB}\, d\lambda\, d\theta}{\int_0^{\infty} I_{\lambda}^{BB}\, d\lambda\, d\theta} = \frac{\int_0^{\infty} E(\lambda)\, I_{\lambda}^{BB}\, d\lambda\, d\theta}{\sigma T_{cover}^4} \tag{2}$$

$$I_{\lambda}^{BB} = \frac{2\hbar c^2}{\lambda^5 \left(e^{\frac{\hbar c}{\lambda K T_{cover}}} - 1\right)} \tag{3}$$

$$EFS_{cover} = \frac{GC_r T_{sol} - T_{BB}\sigma T_{abs}^4 - E_{BB}\sigma T_{cover}^4}{GC_r} \tag{4}$$

Where the parameters in the above equations, λ, G(λ), T(λ), E(λ), I_{λ}^{BB}, T_{cover}, σ, θ, ħ, c, *K*, and C_r represent wavelength (nm), irradiation in the AM1.5 spectrum (W/m^2), the transmittance of the cover (at each wavelength), the emissivity of the cover (at each wavelength), Planck's function, the cover temperature (Kelvin), the Stefan-Boltzmann constant (5.67×10^{-8} W/m^2 K^4), angle (radians), Planck's constant (6.626×10^{-34} m^2 kg/s), the speed of light (2.99×10^8 m/s), Boltzmann constant (1.38×10^{-23}), and the solar concentration ratio, respectively. As emission occurs in all upward directions, (2) must be also integrated over a 2π solid angle. Pulling this all together, T_{sol}, E_{BB}, and EFS (at key operating conditions) of samples are estimated numerically.

To calculate EFS (Eqn. (4)) the absorber temperatures are assumed to be 373.15, 673.15, and 873.15 K; the cover temperature can be estimated using the following:

$$\frac{Q}{A} \times \frac{\delta}{k} = \Delta T = T_{absorber} - T_{cover} \tag{5}$$

where δ and k are the thickness and thermal conductivity of the cover. The ITO-coated cover in this manuscript is made of 1.1×10^{-3} m thick

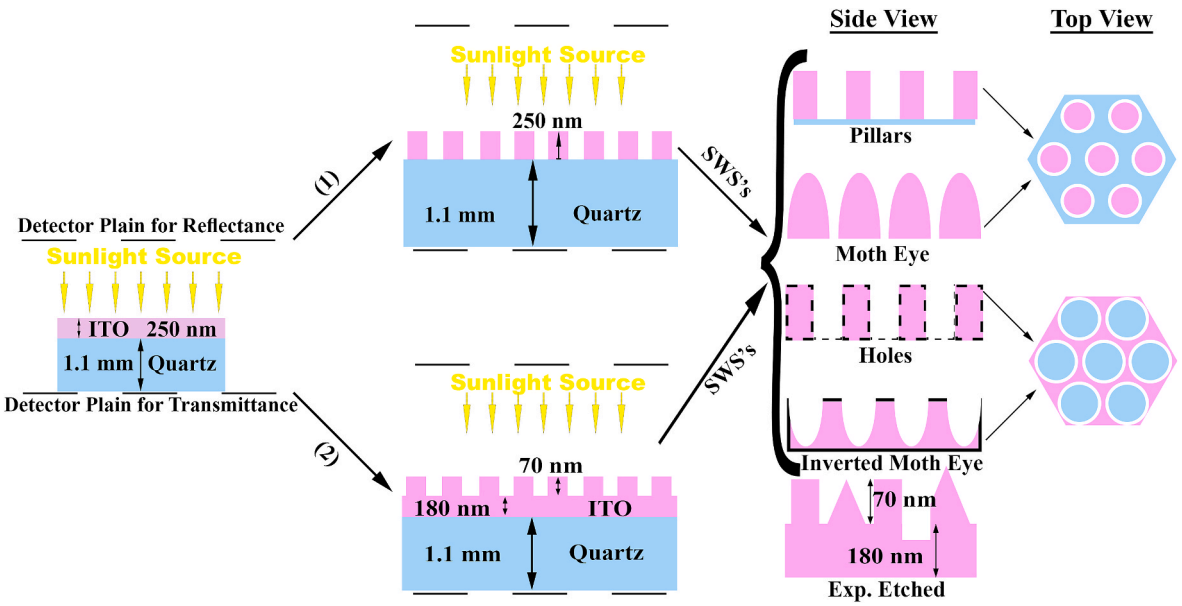

Fig. 2. ITO pattern geometries modelled and the side-view of the experimentally etched sample coated on quartz.

quartz and 250 × 10^{-9} m thick ITO. If the thickness of ITO is overlooked (compared to quartz's), the effective thermal conductivity of the cover at 373.15, 673.15, and 873.15 K are ~1.48, ~1.74, and 1.90 W/m K, respectively [55]. $\frac{Q}{A}$ was assumed to be 20% of the incoming energy (i.e., $C_r \times G$ W/m^2).

3. Results and discussion

3.1. Plain ITO characterisation results

3.1.1. Ellipsometry study for plain ITO optical constants

The ellipsometry results for the current work come from two different measurements and can be subdivided into two overlapping wavelength ranges (e.g., 280-3300 nm and 1600–40,000 nm). The optical constants were modelled in the former region (short wavelengths) using a parametric model combining Tauc-Lorentz + Drude, Gaussian graded profile, and a surface roughness layer similar to Ref. [56], while two Cauchy layers for the substrate and the ITO layer were applied for the latter region (long wavelengths), an approach which was similar to Ref. [57]. To avoid any local minimum, a careful and thorough global search by monitoring MSE was done. The MSE values were ~5 and less than one, for both short and long wavelengths, respectively, which show a good fit. The fitted film thickness in short wavelengths was approximately 248 nm, which corroborates well with the (nominal) thickness provided by the ITO manufacturer, 250 nm. The optical constants for short and long wavelengths are presented in Fig. 3.

Generally, ITO films have a higher refractive index and extinction coefficient than bare quartz, which can be attributed to the presence of dopants and a relatively high density of free carriers [60].

3.1.2. Transmittance and reflectance spectra

The transmission and reflection spectra of the ITO samples (with the ITO-side facing the detector) are presented in Fig. 4.

As can be seen, the reflection of the ITO-coated sample (unetched, ~250 nm thickness, on a 1.1 mm quartz substrate) is higher than the bare quartz substrate at any wavelength smaller than 700 nm. This can be justified by looking at the refractive index of ITO in this range which is higher than the bare substrate (see Fig. 4a). This result suggests that the addition of suitable SWSs can effectively decrease the reflection in this region [24,28]. The lower reflection leads to higher transmission

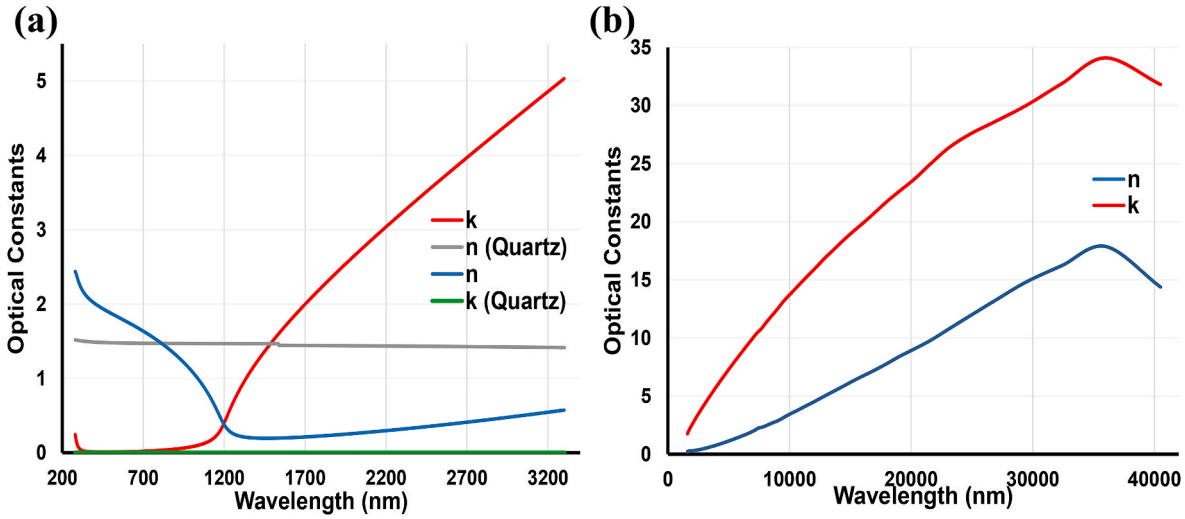

Fig. 3. ITO optical constants: (a) short wavelengths (bare quartz is as a reference [58,59]), (b) long wavelengths.

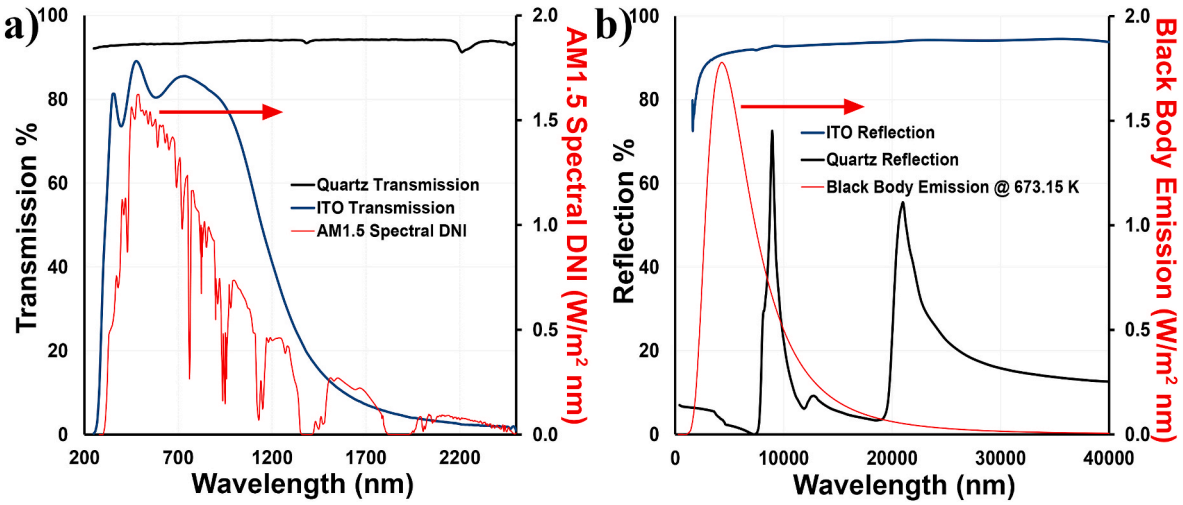

Fig. 4. a) Measured transmission spectra of flat ITO-coated (250 nm thick) quartz sample at short wavelengths (solar spectrum is added for the reference); b) Calculated reflection spectra of flat ITO-coated sample at long wavelengths using OpenFilter (black body emission spectrum is added for the reference).

results and higher energy input to the solar thermal systems. Simultaneously, the selectivity of ITO reduces radiative heat loss from the system, which can boost thermal efficiency [7].

3.1.3. Surface characterisation

As discussed in sub-section **3.1**, the film thickness was confirmed by ellipsometry measurements, which showed a good agreement with the quoted nominal thickness. From this, the surface of the manufactured ITO samples was inspected by several SEM images. No cracks or scratches could be found in the images (see Fig. 5a). Additionally, the surface structure was similar to the available samples in the literature [61]. AFM measurements were also performed on the relatively large area (5 μm × 5 μm) to obtain a surface roughness (RSM, R_q) equal to ~1.96 ± 0.29 nm (see Fig. 5b). This indicates that the unetched ITO film had a high degree of uniformity.

3.2. Deposited etch mask

Following the PS deposition process using DSA technique, the deposition surface was characterised via SEM imaging (see Fig. 6).

Fig. 6 indicates that although the particle size was relatively uniform, there are some gaps and overlapping sections of nanoparticles. The overlapping sections likely result from agglomeration in the suspension phase, which becomes more prevalent for small particles during the DSA process. During the etching process, it is anticipated that the 'gaps' receive the deepest etching while the overlapping areas have little/no etching. To estimate the area fraction of uncoated regions (i.e., gaps between particles), the SEM images were analysed using ImageJ, a free image processing software [62]. The 'gap' area fraction was determined to be ~30%. Please note this 'gap' area fraction for a perfectly deposited hexagonal array etch mask is ~26% [48], so the observed gaps are only a few percentage points greater. For the 'overlapping' sections, the average area fraction was estimated to be ~16%.

3.3. Etching results

Next, the etching recipe (mentioned in Table 2) was carried out. Before and after the etch process, the samples were characterised again using an electron microscope (Fig. 7 provides the results). Importantly, as mentioned in sub-section 2.3.1 a focussed ion beam (FIB) process was applied to the sample to determine the etch depth in Fig. 7e. This etch depth was used as an input to the modelling.

As can be seen in Fig. 7d and e, the resulting nanopatterns (after etching) are stochastic, rather than periodic. The tilted SEM suggests the etching depth is ~70 nm while the AFM analysis indicates that the nanostructures' height is 30–50 nm.

3.4. Modelling results

As noted above, the modelling was used to investigate the real nanopatterned ITO fabricated in this study (on a 1.1 mm of quartz substrate) along with the 'ideal' ITO-based SWS geometry. As such, the aim was to find the most promising SWS designs (including a different etch depth, 70 nm) and to understand the impact of manufacturing flaws

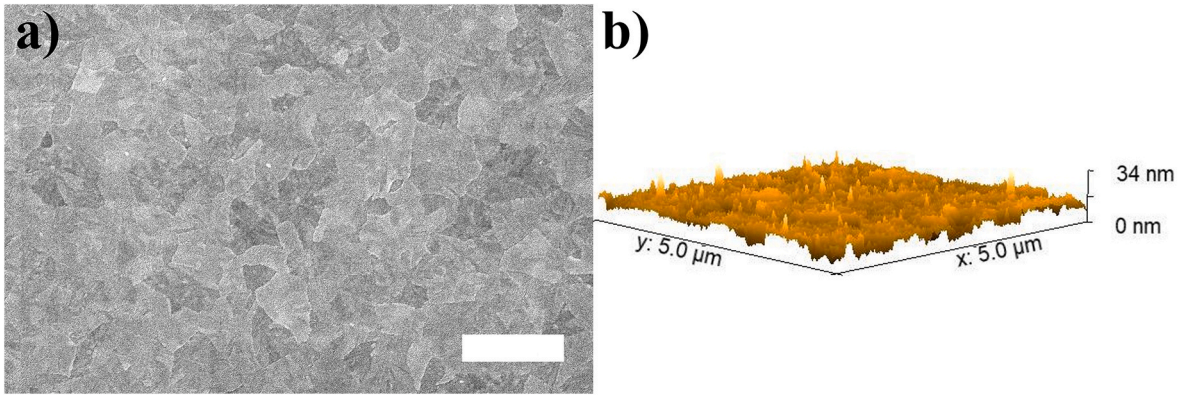

Fig. 5. Surface characterisation a) SEM image (top view of the sample, ITO on top, the scale bar represents 2 μm), b) AFM image of the sample (ITO on top).

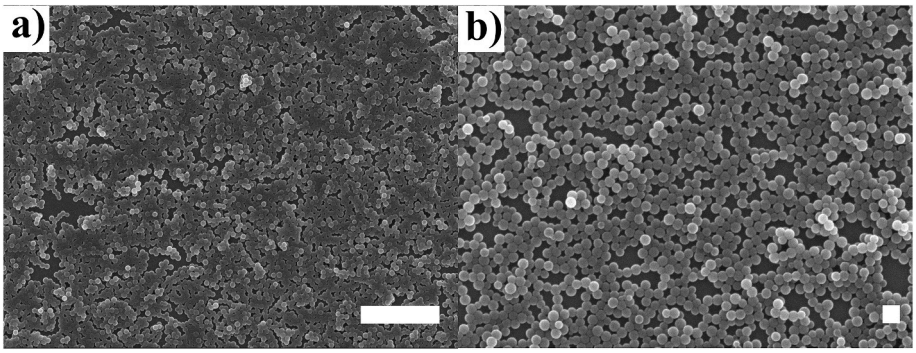

Fig. 6. Selected SEM images of a PS-coated ITO sample: a) top-view (the scale bar is 1 μm) b) top-view (the scale bar is 100 nm).

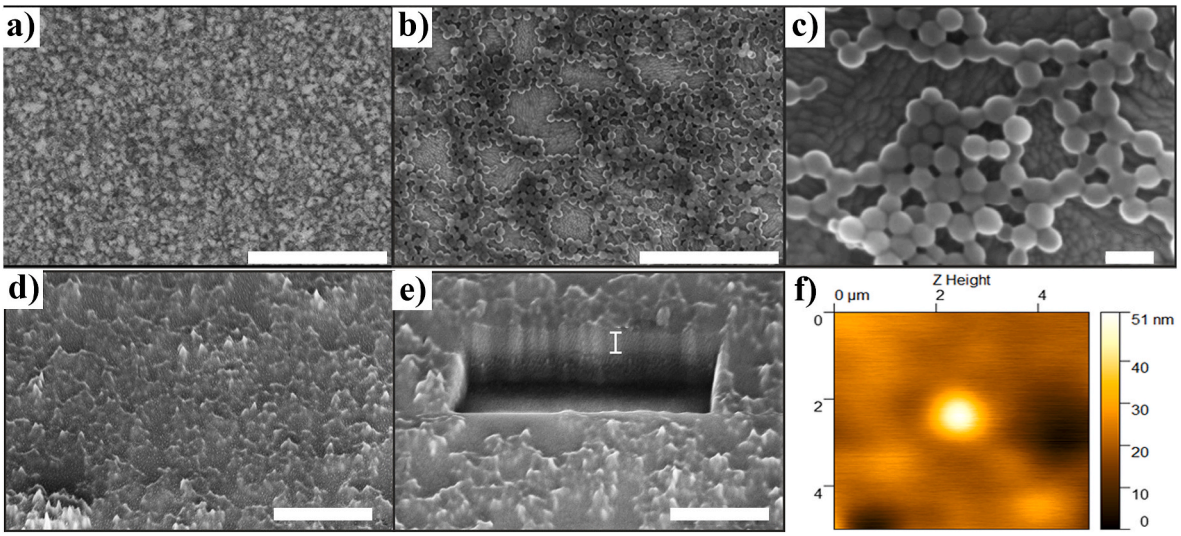

Fig. 7. SEM imaging of a sample before and after etching: a) Before etching (the scale bar is 5 μm); b) Before etching (the scale bar is 1 μm); c) Before etching (the scale bar is 100 nm); d) After 2 min of dry etching (tilted-view of ITO nanostructures on the quartz substrate, the scale bar is 1 μm); e) A tilted-view of the etched sample after a FIB sample preparation to measure the etch depth (the scale bar represents 1 μm while the vertical line is 180 nm), f) AFM image of the sample after the etching.

and inherent surface roughness effects.

Fig. 8a and b depict the modelled reflection spectra of the cases in which the 250 nm ITO layer was fully (i.e., 250 nm deep) and partially (i.e., 70 nm deep) patterned, respectively. The modelled transmission spectra of fully (i.e., 250 nm deep) and partially (i.e., 70 nm deep) patterned ITO cases are illustrated in Fig. 8c and d, respectively. Additionally, the calculated T_{sol} and E_{BB} for both 250 nm and 70 nm deep etched cases are shown in Fig. 8e. The solar weighted transmittance (T_{sol}) was calculated for each case using the data shown in the insets in Fig. 8c and d. Please note for the experimentally etched sample (i.e., 'Exp. Etched) the long wavelength data were assumed to be the same as "Rough Surface" due to lack of FT-IR reflectance and transmittance data. Even though the literature suggests a moth's eye structure with a height of 250 nm can improve light transmission in the visible window [21,26], it was found that setting the height is not enough for this application. So, depending on other factors such as spacing, light with even higher wavelengths (i.e., beyond the visible region) can still interact with these nano features, leading to counterproductive higher transmission at these wavelengths (see Fig. 8c). As can be seen in Fig. 8d the 'rough surface' sample overestimated the transmission of the etched sample at shorter wavelengths (i.e, <2000 nm). This could be attributed to gaps in the prepared etch mask which can cause irregular shapes and internal reflections (read: higher absorption). Fig. 8e, suggests that a patterned surface with nanoholes (height = 250 nm and spacing = 60 nm) can give a T_{sol} comparable to that of the bare substrate and also slightly decreases the emittance (E_{BB}) compared to the unetched ITO-coated case. However, the decrease in E_{BB} is at the expense of increasing blackbody-weighted transmission (T_{BB}), meaning more heat can transmit through the cover despite the lower emittance of the case. As noted above EFS metric does a better job of comparing the options for the application, which is presented in Table 3. Also, among the 70 nm-studied cases the best solar weighted light transmission (T_{sol} = ~0.85) is for a sample with inverted moth eye structures (height = 70 nm and spacing = 30 nm).

The calculation of E_{BB} and EFS were done for 'Exp. Etched' assuming its transmittance and reflectance properties behave the same 'Rough Surface' (based upon microscopy images) in Fig. 8e and Table 3. Based on the results in Table 3 and Fig. 8e the following recommendations can be made regarding overall performance.

- At $C_r = 1$ (@ 100 °C) four cases perform better than the unetched ITO (and of course the bare quartz), the inverted moth eye (height = 250 nm & spacing = 80 nm), the holes (height = 250 nm & spacing = 90 nm), the inverted moth eye (height = 70 nm & spacing = 30), and the moth eye (height = 70 & spacing = 30 nm) resulting in ~7, ~9, ~7, and ~3% boost in $T_{sol,}$ respectively.
- At $C_r = 10$ (@ 400 °C) both partially etched (i.e., height = 70 nm and spacing = 30 nm) and fully etched (height = 250 nm and spacing = 80 nm) inverted moth eye cases are the top performing ones, improving T_{sol} by ~7 and ~8%, respectively.

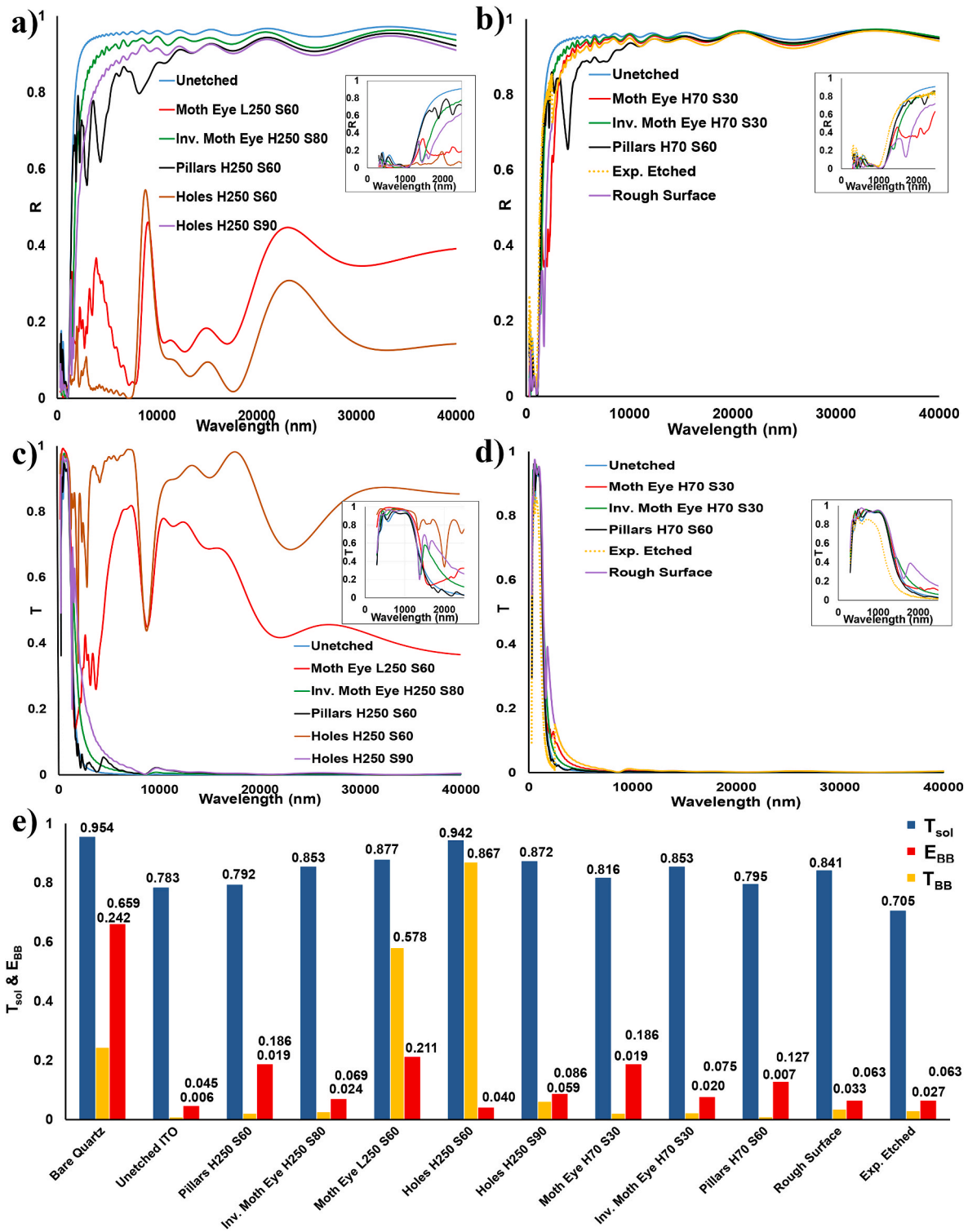

Fig. 8. Modelling and experimental results: a) Reflectance results of the fully etched cases; b) The experimental reflectance and the modelled reflectance results of the comparative study (i.e., etched ITO thickness is 70 nm) (NB: the reflectance of 'Exp. Etched' was assumed to be the same as 'Rough Surface' at long wavelengths. The unetched sample spectra were added as references); c) Transmittance results of the fully etched cases; d) Transmittance results of the experimentally etched sample (NB: the transmittance of 'Exp. Etched' was assumed to be the same as 'Rough Surface' at long wavelengths) together with the cases of comparative study. e) Solar-weighted transmittance, emittance (@ 400 °C), and blackbody-weighted transmittance (@ 400 °C) of the cases if the ITO layer could be fully patterned (in the z-direction) & the cases in the comparative study (the results for bare quartz and unetched ITO were added as the baselines).

- At $C_r = 100$ (@ 600 °C) the results suggest that the inverted moth eye (height = 250 nm and spacing = 80 nm) marginally beats the holes (height = 250 and spacing = 90 nm) leading to ~7% relative boost in EFS and ~8% in T_{sol}.

Even though the fabrication of pillars should be easier, the etched cases were not as promising as the moth eye structures, when EFS was considered along with T_{sol}. However, some manufacturing balance is needed because cost represents a key limiting factor for bringing micro/

Table 3
EFS results for all the modelled cases at three different solar concentrations, 1, 10, and 100. Bare quartz and unetched ITO-coated quartz are also added as reference cases.

Cases		$C_r = 1$ (@ 100 °C)	$C_r = 10$ (@ 400 °C)	$C_r = 100$ (@ 600 °C)
Bare Quartz		0.0443	−0.0889	0.6589
Unetched ITO (*Target to Beat*)		0.7362	0.7235	0.7624
Exp. Etched		0.6372	0.6001	0.6683
70 nm etched ITO on top of 180 nm ITO	**Moth Eye H70 S30**	0.7565	0.7056	0.7681
	Inv. Moth Eye H70 S30	0.7656	0.7416	0.7914
	Pillars H70 S60	0.7096	0.6403	0.7443
250 nm	**Moth Eye L250 S60**	0.0330	−0.0401	0.6219
	Inv. Moth Eye H250 S80	0.7820	0.7460	0.8131
	Pillars H250 S60	0.6544	0.5547	0.7155
	Holes H250 S60	0.0208	−0.1132	0.6385
	Holes H250 S90	0.7700	0.7038	0.8085

nano-fabricated materials and components to renewable energy systems. Most nanofabrication techniques are inherently hard to scale (as batch processes) and often require cleanrooms [63]. However, the proposed experimental process (i.e., double self-assembly) provides a potentially scalable pathway towards a low specific cost process. If this technology can be scaled and extended moth eye structures, the added cost of such patterning may eventually be justified by the ~7% optical performance boost over a typical ~25-year life.

4. Conclusions and outlook

This work proposes that nanopatterned, selective ITO covers can be designed and fabricated to simultaneously provide low emission (long wavelength radiative heat loss) and high (short wavelength) solar transmission for solar thermal collectors (compared to a flat ITO-coated cover). The investigation described above used both experimental synthesis and characterisation as well as FDTD simulations (based on measured ITO optical properties). From the experimental perspective, a deposition etch mask made of polystyrene nanospheres was prepared using the DSA technique. This mask was then dry-etched, characterised, and analysed. At the same time, numerous alternative geometries/patterns were simulated and compared to the as-produced sample using an overall metric, the efficiency factor for selectivity. The main contributions of this study are the following.

- Experimentally, an etch mask of ~60 nm polystyrene nanospheres was produced successfully, which is among the smallest in the literature (if not the smallest).
- The as-produced sample achieved a $T_{sol} = 0.705$, $E_{BB} = 0.075$, and EFS = 0.6680 (at best conditions)
- From the simulations, it was confirmed that although structural features much smaller than the desired wavelength cut off can be "invisible" to those greater wavelengths, the scale and shape of the air gaps are also important to ensure the final optical properties are as desired.
- The inverted moth eye pattern (height = 250 nm and spacing = 80 nm) was found to give the best result among the studied cases at all three solar concentrations 1, 10, and 100 suns, resulting in ~6, ~3, and ~7% relative boost in EFS, respectively and ~7% improvement in T_{sol}.

From an experimental aspect, the synthesis method can likely be improved in future work by employing "block co-polymer (BCP) lithography" to have better control over spacing. From modelling perspective, there are several geometric refinements that could be included in future studies to optimise the design for the exact operation conditions (e.g., the solar concentrations ratio and operating temperatures). Another important, yet unchecked, potential feature of patterned ITO designs is that they may have a self-cleaning function (like other micro/nanopatterned geometries in the literature). Overall, though, it can be concluded that it is indeed possible to get a net performance boost for solar thermal collector covers through careful design and synthesis of nanopatterned ITO.

CRediT authorship contribution statement

Mahdi Motamedi: Conceptualization, Methodology, Validation, Formal analysis, Investigation, Writing – original draft, Visualization, Project administration. **Guobin Jia:** Formal analysis, Investigation, Writing – original draft. **Yin Yao:** Formal analysis, Investigation. **Katie Shanks:** Data curation, Resources, Software, Visualization, Writing – original draft, Writing – review & editing. **Peyman Yousefi:** Formal analysis, Resources, Investigation, Writing – original draft. **Yasitha L. Hewakuruppu:** Data curation, Resources, Software. **Mehdi Rafeie:** Data curation, Visualization, Software. **Florian Lindner:** Formal analysis, Investigation, Resources. **Robert Patterson:** Resources, Supervision, Writing – review & editing. **Silke Christiansen:** Resources, Supervision, Writing – original draft, Writing – review & editing. **Jonathan Plentz:** Resources, Supervision, Writing – original draft, Writing – review & editing. **Pramod Koshy:** Resources, Supervision, Writing – original draft, Writing – review & editing. **Robert A. Taylor:** Resources, Supervision, Writing – original draft, Conceptualization, Writing – review & editing.

Declaration of competing interest

The authors declare that they have no known competing financial interests or personal relationships that could have appeared to influence the work reported in this paper.

Acknowledgements

MM acknowledges the Australian Government for Research Training Program Scholarship (HDR Completion Scholarship). MM would like to thank Yuanchih (Atom) Chang (SPREE UNSW, Australia), Mark Gross, Joanna Szymanska, Pierrette Michaux, and Andrew See (ANFF NSW, Australia) for sharing their experience with etch mask preparation. The LB trough and its training at SPREE UNSW were kindly provided by Shujuan Huang (currently with Macquarie University) and Pengfei Zhang, respectively. Ute Schubert (ANFF NSW) is thanked for giving access to Complete EASE software. MM expresses his gratitude to Kensuke Kanada et al. (GEOMATEC, Japan) for ITO fabrication. Thanks are extended to Simon Doe (Future Industries UniSA, Australia) and Fouad Karouta (ANFF ACT, Australia) for their assistance to find a suitable fabrication partner within Australia. Katie McBean and Geoffrey McCredie (MAU at UTS, Australia), and Elena Kosobrodova (USYD, Australia) are also acknowledged for assistance in ellipsometric measurements of ITO samples. Andrea Dellith & Jan Dellith, Barbara Geisenhainer (from Leibniz IPHT, Germany), and Lamborghini Sotelo (from IKTS, Germany) are thanked for their assistance with SEM imaging, FT-IR and the optical measurements of the etched sample, and AFM imaging, respectively. This work was performed in part at the NSW Node of the Australian National Fabrication Facility.

References

[1] A. Whillier, Plastic covers for solar collectors, Sol. Energy 7 (3) (1963) 148–151.

[2] J.A. Duffie, W.A. Beckman, Solar Engineering of Thermal Processes, fourth ed., John Wiley & Sons, 2013.
[3] R. Bakari, R.J. Minja, K.N. Njau, Effect of glass thickness on performance of flat plate solar collectors for fruits drying, J. Energy 2014 (2014).
[4] M. Rubin, Optical properties of soda lime silica glasses, Sol. Energy Mater. 12 (1985) 275–288.
[5] C.G. Granqvist, Transparent conductors as solar energy materials: a panoramic review, Sol. Energy Mater. Sol. Cells 91 (17) (2007) 1529–1598.
[6] M. Motamedi, C.-Y. Chung, M. Rafeie, N. Hjerrild, F. Jiang, H. Qu, R.A. Taylor, Experimental testing of hydrophobic microchannels, with and without nanofluids, for solar PV/T collectors, Energies 12 (15) (2019) 3036.
[7] R.A. Taylor, Y. Hewakuruppu, D. DeJarnette, T.P. Otanicar, Comparison of selective transmitters for solar thermal applications, Appl. Opt. 55 (14) (2016) 3829–3839.
[8] Y. Hewakuruppu, Investigating the Potential of Developing a Selective Nanofluid-Based Direct Absorption Solar Collector, School of Mechanical and Manufacturing Engineering, University of New South Wales, Sydney, 2016.
[9] H. Jia, T. Matsui, M. Kondo, Enhanced infrared transmission of GZO film by rapid thermal annealing for Si thin film solar cells, Prog. Photovoltaics Res. Appl. 20 (1) (2012) 111–116.
[10] F. Lungwitz, R. Escobar-Galindo, D. Janke, E. Schumann, R. Wenisch, S. Gemming, M. Krause, Transparent conductive tantalum doped tin oxide as selectively solar-transmitting coating for high temperature solar thermal applications, Sol. Energy Mater. Sol. Cells 196 (2019) 84–93.
[11] F. Giovannetti, S. Föste, N. Ehrmann, G. Rockendorf, High Transmittance, Low Emissivity Glass Covers for Flat Plate Collectors: Applications and Performance, Energy Procedia, 2012, pp. 106–115.
[12] F. Giovannetti, S. Föste, N. Ehrmann, G. Rockendorf, High transmittance, low emissivity glass covers for flat plate collectors: applications and performance, Sol. Energy 104 (2014) 52–59.
[13] S. Krause, P.T. Miclea, F. Steudel, S. Schweizer, G. Seifert, Precise microstructuring of indium-tin oxide thin films on glass by selective femtosecond laser ablation, EPJ Photovoltaics 4 (2013).
[14] M. Shimizu, F. Iguchi, H. Yugami, High-temperature solar selective absorbers based on interface effects in refractory metals coated with transparent conductive oxides, in: ASME 2012 6th International Conference on Energy Sustainability, ES 2012, Collocated with the ASME 2012 10th International Conference on Fuel Cell Science, Engineering and Technology, 2012, pp. 423–428.
[15] M. Shimizu, M. Suzuki, F. Iguchi, H. Yugami, High-temperature Solar Selective Absorbers Using Transparent Conductive Oxide Coated Metal, Energy Procedia, 2014, pp. 418–426.
[16] M. Shimizu, M. Suzuki, A. Kohiyama, F. Iguchi, H. Yugami, Application of Transparent Conductive Oxides Films for High-Temperature Solar Selective Absorbers, ASME 2014 8th International Conference on Energy Sustainability, ES 2014 Collocated with the ASME 2014 12th International Conference on Fuel Cell Science, Engineering and Technology, 2014.
[17] M. Shimizu, T. Abe, F. Iguchi, H. Yugami, High-temperature solar selective absorbers based on a transparent conductive oxide film coated periodic micro-hole array, AIP Conf. Proc. 1850 (1) (2017) 12003.
[18] M. Shimizu, M. Suzuki, F. Iguchi, H. Yugami, High spectral selectivity for solar absorbers using a monolayer transparent conductive oxide coated on a metal substrate, J. Appl. Phys. 121 (18) (2017).
[19] Q. Wang, M. Hu, H. Yang, J. Cao, J. Li, Y. Su, G. Pei, Performance evaluation and analyses of novel parabolic trough evacuated collector tubes with spectrum-selective glass envelope, Renew. Energy 138 (2019) 793–804.
[20] R.A. Taylor, Y. Hewakuruppu, D. Dejarnette, T.P. Otanicar, Fabrication and Comparison of Selective, Transparent Optics for Concentrating Solar Systems, Proceedings of SPIE - The International Society for Optical Engineering, 2015.
[21] A. Taylor, I. Parkin, N. Noor, C. Tummeltshammer, M.S. Brown, I. Papakonstantinou, A bioinspired solution for spectrally selective thermochromic VO 2 coated intelligent glazing, Opt Express 21 (105) (2013) A750–A764.
[22] A. Gombert, W. Glaubitt, K. Rose, J. Dreibholz, B. Bläsi, A. Heinzel, D. Sporn, W. Döll, V. Wittwer, Subwavelength-structured antireflective surfaces on glass, Thin Solid Films 351 (1) (1999) 73–78.
[23] O. Deparis, S. Mouchet, L. Dellieu, J.F. Colomer, M. Sarrazin, Nanostructured surfaces: bioinspiration for transparency, coloration and wettability, Mater. Today: Proc. (2014) 122–129.
[24] J. Cai, L. Qi, Recent advances in antireflective surfaces based on nanostructure arrays, Mater. Horiz. 2 (1) (2015) 37–53.
[25] N. Das, S.I. Sen, Optimization of nano-grating structure to reduce the reflection losses in gaas solar cells, 2012 22nd australasian universities power engineering conference: "green smart grid systems, in: AUPEC 2012, 2012.
[26] M. Motamedi, M.E. Warkiani, R.A. Taylor, Transparent surfaces inspired by nature, Adv. Opt. Mater. (2018), 1800091.
[27] S. Chattopadhyay, Y.F. Huang, Y.J. Jen, A. Ganguly, K.H. Chen, L.C. Chen, Anti-reflecting and photonic nanostructures, Mater. Sci. Eng. R Rep. 69 (1–3) (2010) 1–35.
[28] P. Clapham, M. Hutley, Reduction of lens reflexion by the “Moth Eye” principle, Nature 244 (5414) (1973) 281–282.
[29] S. Wilson, M. Hutley, The optical properties of'moth eye'antireflection surfaces, J. Mod. Opt. 29 (7) (1982) 993–1009.
[30] A. Peter Amalathas, M.M. Alkaisi, Nanostructures for light trapping in thin film solar cells, Micromachines 10 (9) (2019) 619.
[31] P.C. Tseng, M.A. Tsai, P. Yu, H.C. Kuo, Antireflection and light trapping of subwavelength surface structures formed by colloidal lithography on thin film solar cells, Prog. Photovoltaics Res. Appl. 20 (2) (2012) 135–142.
[32] Y.-R. Lin, H.-P. Wang, C.-A. Lin, J.-H. He, Surface profile-controlled close-packed Si nanorod arrays for self-cleaning antireflection coatings, J. Appl. Phys. 106 (11) (2009), 114310.
[33] M. Henry, P.M. Harrison, J. Wendland, Rapid Laser Patterning of ITO on Glass for Next Generation Plasma Display Panel Manufacture, Digest of Technical Papers - SID International Symposium, 2007, pp. 1209–1212.
[34] H.K. Raut, V.A. Ganesh, A.S. Nair, S. Ramakrishna, Anti-reflective coatings: a critical, in-depth review, Energy Environ. Sci. 4 (10) (2011) 3779–3804.
[35] D.S. Leem, T. Lee, T.Y. Seong, Enhancement of the light output of GaN-based light-emitting diodes with surface-patterned ITO electrodes by maskless wet-etching, Solid State Electron. 51 (5) (2007) 793–796.
[36] K. Fouad, A practical approach to reactive ion etching, J. Phys. D Appl. Phys. 47 (23) (2014), 233501.
[37] M. Park, C. Harrison, P.M. Chaikin, R.A. Register, D.H. Adamson, Block copolymer lithography: periodic arrays of ~1011 holes in 1 square centimeter, Science 276 (5317) (1997) 1401–1404.
[38] C. Tang, E.M. Lennon, G.H. Fredrickson, E.J. Kramer, C.J. Hawker, Evolution of block copolymer lithography to highly ordered square arrays, Science 322 (5900) (2008) 429–432.
[39] Q. Xie, M. Hong, H. Tan, G. Chen, L. Shi, T. Chong, Fabrication of nanostructures with laser interference lithography, J. Alloys Compd. 449 (1–2) (2008) 261–264.
[40] J.C. Hulteen, R.P. Van Duyne, Nanosphere lithography: a materials general fabrication process for periodic particle array surfaces, J. Vac. Sci. Technol. A: Vacuum, Surfaces, and Films 13 (3) (1995) 1553–1558.
[41] G. Jia, J. Plentz, M. Presselt, J. Dellith, A. Dellith, S. Patze, F.J. Tölle, R. Mülhaupt, G. Andrä, F. Falk, A double self-assembly process for versatile reduced-graphene-oxide layer deposition and conformal coating on 3D structures, Adv. Mater. Interfac. 4 (23) (2017), 1700758.
[42] G. Jia, J. Westphalen, J. Drexler, J. Plentz, J. Dellith, A. Dellith, G. Andrä, F. Falk, Ordered silicon nanowire arrays prepared by an improved nanospheres self-assembly in combination with Ag-assisted wet chemical etching, Photon. Nanostruct: Fundam. Appl. 19 (2016) 64–70.
[43] R. Arat, G. Jia, J. Plentz, Low temperature chemical treatment of graphene films made by double self-assembly process to improve sheet resistance, Diam. Relat. Mater. 111 (2021), 108218.
[44] P.I. Stavroulakis, N. Christou, D. Bagnall, Improved deposition of large scale ordered nanosphere monolayers via liquid surface self-assembly, Mater. Sci. Eng., B 165 (3) (2009) 186–189.
[45] K. Wostyn, Y. Zhao, B. Yee, K. Clays, A. Persoons, G. de Schaetzen, L. Hellemans, Optical properties and orientation of arrays of polystyrene spheres deposited using convective self-assembly, J. Chem. Phys. 118 (23) (2003) 10752–10757.
[46] K. Han, C.-H. Chang, Numerical modeling of sub-wavelength anti-reflective structures for solar module applications, Nanomaterials 4 (1) (2014) 87–128.
[47] M.M. Braun, L. Pilon, Effective optical properties of non-absorbing nanoporous thin films, Thin Solid Films 496 (2) (2006) 505–514.
[48] D. Stavenga, S. Foletti, G. Palasantzas, K. Arikawa, Light on the moth-eye corneal nipple array of butterflies, Proc. R. Soc. Lond. B Biol. Sci. 273 (1587) (2006) 661–667.
[49] D.A.G. Bruggeman, Berechnung verschiedener physikalischer Konstanten von heterogenen Substanzen. I. Dielektrizitätskonstanten und Leitfähigkeiten der Mischkörper aus isotropen Substanzen, Ann. Phys. 416 (7) (1935) 636–664.
[50] K. Choi, J. Jung, J. Kim, J. Lee, H.S. Lee, I.-S. Kang, Antireflective transparent conductive oxide film based on a tapered porous nanostructure, Micromachines 11 (2) (2020) 206.
[51] R. Bouffaron, L. Escoubas, J. Simon, P. Torchio, F. Flory, G. Berginc, P. Masclet, Enhanced antireflecting properties of microstructured top-flat pyramids, Opt Express 16 (23) (2008) 19304–19309.
[52] T. Minami, Transparent conducting oxide semiconductors for transparent electrodes, Semicond. Sci. Technol. 20 (4) (2005) S35.
[53] C.-L. Tien, H.-Y. Lin, C.-K. Chang, C.-J. Tang, Effect of oxygen flow rate on the optical, electrical, and mechanical properties of dc sputtering ITO thin films, Adv. Condens. Matter Phys. (2018) 2018.
[54] C. Xu, L. Deng, A. Holder, L.R. Bailey, C. Leendertz, J. Bergmann, G. Proudfoot, O. Thomas, R. Gunn, M. Cooke, Nanoparticle and nanosphere mask for etching of ITO nanostructures and their reflection properties, Physica Status Solidi (A) Applications and Materials Science 212 (1) (2015) 171–176.
[55] O. Sergeev, A. Shashkov, A. Umanskii, Thermophysical properties of quartz glass, J. Eng. Phys. 43 (6) (1982) 1375–1383.
[56] T. Stoica, M. Gartner, M. Losurdo, V. Teodorescu, M. Blanchin, T. Stoica, M. Zaharescu, Spectroellipsometric study of the sol–gel nanocrystalline ITO multilayer films, Thin Solid Films 455 (2004) 509–512.
[57] R. Synowicki, Spectroscopic ellipsometry characterization of indium tin oxide film microstructure and optical constants, Thin Solid Films 313 (1998) 394–397.
[58] Optical constants of SiO2 (silicon dioxide, silica, quartz) - lemarchand 2013: thin film; n,k 0.25-2.5 µm. https://refractiveindex.info/?shelf=main&book=SiO2&page=Lemarchand. (Accessed 8 September 2020).
[59] Optical constants of SiO2 (Silicon dioxide, Silica, Quartz) Kischkat et al. 2012: thin film; n,k 1.54-14.3 µm. https://refractiveindex.info/?shelf=main&book=SiO2&page=Kischkat. (Accessed 22 October 2020).
[60] Y.S. Jung, Spectroscopic ellipsometry studies on the optical constants of indium tin oxide films deposited under various sputtering conditions, Thin Solid Films 467 (1–2) (2004) 36–42.

[61] D.P. Pham, B.T. Phan, V.D. Hoang, H.T. Nguyen, T.K.H. Ta, S. Maenosono, C. V. Tran, Control of preferred (222) crystalline orientation of sputtered indium tin oxide thin films, Thin Solid Films 570 (2014) 16–19.

[62] M.D. Abràmoff, P.J. Magalhães, S.J. Ram, Image processing with ImageJ, Biophot. Int. 11 (7) (2004) 36–42.

[63] M.A. Butt, Thin-film coating methods: a successful marriage of high-quality and cost-effectiveness—a brief exploration, Coatings 12 (8) (2022) 1115.